The Astrophysical Journal, 745:36 (9pp), 2012 January 20 doi:10.1088/0004-637X/745/1/36

DISCONNECTING OPEN SOLAR MAGNETIC FLUX

C. E. DeForest[1], T. A. Howard[1], and D. J. McComas[1,2]
[1] Southwest Research Institute, 1050 Walnut Street Suite 300, Boulder, CO 80302, USA
[2] Department of Physics and Astronomy, University of Texas at San Antonio, San Antonio, TX 78249, USA
Received 2011 September 30; accepted 2011 November 30; published 2011 December 28

ABSTRACT

Disconnection of open magnetic flux by reconnection is required to balance the injection of open flux by coronal mass ejections and other eruptive events. Making use of recent advances in heliospheric background subtraction, we have imaged many abrupt disconnection events. These events produce dense plasma clouds whose distinctive shape can now be traced from the corona across the inner solar system via heliospheric imaging. The morphology of each initial event is characteristic of magnetic reconnection across a current sheet, and the newly disconnected flux takes the form of a "U-"shaped loop that moves outward, accreting coronal and solar wind material. We analyzed one such event on 2008 December 18 as it formed and accelerated at 20 m s^{-2} to 320 km s^{-1}, thereafter expanding self-similarly until it exited our field of view 1.2 AU from the Sun. From acceleration and photometric mass estimates we derive the coronal magnetic field strength to be 8 μT, 6 $R_\odot$ above the photosphere, and the entrained flux to be 1.6×10^{11} Wb (1.6×10^{19} Mx). We model the feature's propagation by balancing inferred magnetic tension force against accretion drag. This model is consistent with the feature's behavior and accepted solar wind parameters. By counting events over a 36 day window, we estimate a global event rate of 1 day^{-1} and a global solar minimum unsigned flux disconnection rate of 6×10^{13} Wb yr^{-1} (6×10^{21} Mx yr^{-1}) by this mechanism. That rate corresponds to ~ -0.2 nT yr^{-1} change in the radial heliospheric field at 1 AU, indicating that the mechanism is important to the heliospheric flux balance.

Key words: magnetic reconnection – Sun: corona – Sun: heliosphere – techniques: image processing – techniques: photometric

Online-only material: color figure

1. INTRODUCTION

The solar dynamo generates magnetic flux inside the Sun, which is transported outward and emerges through the Sun's surface into the corona. Magnetic loops build up "closed" magnetic flux (connected to the Sun at both ends) in the corona. Some of these closed loops subsequently "open" into interplanetary space—that is, they are connected to the Sun at only one end with the other extending to great distances in the heliosphere or beyond. Owing to the very high electrical conductivity, open magnetic flux is frozen into the solar wind and carried out with it. The magnetized solar wind expands continuously outward from the Sun in all directions, filling and inflating our heliosphere and protecting the inner solar system from the vast majority of galactic cosmic rays. The balance between the opening and closing of magnetic flux from the Sun is thus critical and fundamental both to the solar wind and to the radiation environment of our solar system.

Magnetic flux opens when coronal mass ejections (CMEs) erupt through the corona, carrying previously closed magnetic loops beyond the critical point where the solar wind exceeds the Alfvén speed (typically $< 20\,R_\odot$) and can no longer return to the Sun. CMEs were first studied in *OSO-7* and *Skylab* observations of the corona (e.g., Tousey 1973; Gosling et al. 1974; Hundhausen 1993), and since then continued work has provided an increasingly detailed picture of these transient magnetic structures both during their formation and ejection, and as they continue to evolve and interact with the solar wind.

Long lasting, radial "legs" are often observed along the flanks of a CME and persisting behind it. These legs are generally interpreted as evidence for at least some continued magnetic connection of CMEs back to the Sun and hence the opening of new magnetic flux with CME ejections. That picture is further supported by observation, in situ, of beamed suprathermal halo electrons streaming in both directions along the local interplanetary magnetic field (IMF) during the passage of an interplanetary CME (ICME) cloud (e.g., Gosling 1990, 1993, and references therein), which are commonly interpreted as signatures of direct connection of the ICME magnetic field to the solar corona in both directions, and hence of newly opening magnetic flux. However, less is known about the equally necessary process of disconnection that must be present to remove newly opened flux and prevent the IMF from growing without limit.

Because of the continual opening of magnetic flux through CMEs, McComas and coworkers in the early 1990s pursued a series of studies to determine how magnetic flux could be closed back off and avoid a so-called magnetic flux "catastrophe" of ever increasing magnetic field strength in the IMF (McComas 1995, and references therein). The amount of open magnetic flux in interplanetary space can be approximated with the "total flux integral" which removes the effects of variations in the solar wind speed in determining the amount of magnetic flux crossing 1 AU (McComas et al. 1992a). Using this integral, McComas et al. (1992a, 1995) showed that if all counterstreaming electron events represent simply connected opening magnetic loops, then for solar maximum CME rates, the amount of flux crossing 1 AU would double over only ~9 months. For flux rope CMEs, significantly more magnetic flux may be observed in the loops crossing 1 AU than what remains attached to the Sun along the CMEs' legs; however, it must be stressed that if CMEs retain any solar attachment whatsoever, the flux catastrophe will ultimately occur in the absence of some other process to close off previously open fields.

Of course a magnetic flux catastrophe is not observed in the solar wind and, in fact, the overall magnitude of the

IMF and amount of open flux seem to vary over the solar cycle. For cycle 21, the average magnitude varied by ∼50% (Slavin et al. 1986) while the total flux integral varied by ∼60% (McComas et al. 1992a, 1992b), with maxima shortly after solar maximum and minima shortly after solar minimum (McComas 1994). Since these studies, the solar wind has gone through a prolonged (multi-cycle) reduction in both solar wind power (the dynamic pressure of the solar wind that ultimately inflates the heliosphere; McComas et al. 2008) and magnetic field magnitude (Smith & Balogh 2008). The lack of a flux catastrophe, solar cycle variation and now long-term reduction in the open magnetic flux from the Sun all show that there must be some process for closing off previously open field regions and returning magnetic flux to the Sun.

Magnetic reconnection plays an important role in regulating the topology of solar magnetic flux. Once the top of a loop passes the critical point, its magnetic flux remains open until some other process occurs to close it off below the critical point. That is, reconnection above the critical point can only rearrange the topology of open magnetic flux in the heliosphere—only reconnection between two oppositely directed (inward and outward field) regions of open flux close to the Sun can close off previously open magnetic flux. The most obvious method of reducing the amount of magnetic flux open to interplanetary space is via reconnection between oppositely directed, previously open field lines (McComas et al. 1989), which creates closed field loops that can return to the Sun and the release of disconnected U-shaped field structures into interplanetary space. An example of such a coronal disconnection event was shown by McComas et al. (1991) using *Solar Maximum Mission* (*SMM*) coronagraph images from 1989 June 1. An even older example of a likely coronal disconnection event can be found as far back as the 1893 April 16 solar eclipse (e.g., Cliver 1989), where sketches (data in 1893) made in time ordered sequence from Chile, Brazil, and Senegal indicate the outward motion of a large U-shaped structure (McComas 1994).

For the opening and closing of the solar magnetic flux to maintain some sort of equilibrium, there must be some type of feedback between these two processes. McComas et al. (1989, 1991) suggested that this feedback occurs through transverse magnetic pressure in the corona, where the expansion of newly opened field regions must enhance transverse pressure and compress already open flux elsewhere around the Sun. When enough pressure builds up, reconnection between oppositely direct open flux would reduce the pressure and amount of open flux. The sequence of images from the 1988 June 27 coronal disconnection event, in fact, showed just such a compression, indicated by the deflection of the streamers in the corona, just prior to and appearing to precipitate the coronal disconnection event. Another line of supporting evidence was provided by numerical simulations (Linker et al. 1992), which indicated that increased magnetic pressure could lead to reconnection across a helmet streamer and the release of disconnected flux. Schwadron et al. (2010) recently reexamined the flux balance issue in light of the anomalously long solar minimum between cycles 23 and 24 and modeled the level of magnetic flux in the inner heliosphere as a balance of that flux injected by CMEs, lost through disconnection, and closed flux lost through interchange reconnection near the Sun.

McComas et al. (1992c) conducted a statistical study of three months of *SMM* coronagraph observations (Hundhausen 1993) to assess the frequency of coronal disconnection events. These authors found that while the initial survey (St. Cyr & Burkepile 1990) found no obvious disconnections, 6 of the 53 transient events during this interval (11%) showed some evidence of disconnection in more than one frame and 13 (23%) showed a single frame with an outward "U" or "V" structure. Given the imaging and analysis technology of the day, McComas et al. (1992c) concluded that magnetic disconnection events on previously open field lines may be far more common than previously appreciated. With today's imaging and exceptional analysis capabilities, the question of coronal disconnection events should finally be resolvable.

For this study we used image sequences, collected by the SECCHI (Howard et al. 2008) instrument suite on board NASA's *STEREO A* spacecraft, of Thomson-scattered sunlight from free electrons in the interplanetary plasma. The observations span from the deep solar corona to beyond 1 AU at elongation angles of up to 70° from the solar disk; this continuous observation is enabled by recently developed background subtraction techniques (DeForest et al. 2011) operating on the *STEREO* data. The signature U-shaped loops of disconnected plasma are far clearer in the processed heliospheric data far from the Sun than in the coronagraph data close to the Sun, and we detect 12 characteristic departing "V" or "U" events in 36 days—far more than the expected number based on scaling the results of McComas et al. (1992c). For this initial report, we focus on quantitative analysis of a single event. In Sections 2.1–2.7, we describe the observations and calculate the geometry, the mass evolution, and (by assuming the U-loop is accelerated by the tension force) the coronal magnetic fields and entrained flux in the disconnecting structure. As a plausibility check, we explore the tension force scenario and its consequences for the long-term evolution of the feature and find that the scenario is consistent with accepted values for the solar wind density and speed. In Section 3, we explore broader consequences of the observation, including estimating the disconnection rate based on the number of similar events in our data set, and discuss implications for the global magnetic flux balance.

2. OBSERVATIONS

The SECCHI suite on *STEREO* was intended to be used as a single integrated imaging instrument (e.g., Howard et al. 2008). It consists of an EUV imager observing the disk of the Sun, and four visible light imagers (COR-1, COR-2, HI-1, and HI-2) with progressively wider overlapping fields of view, to cover the entire range of angles between the solar disk and the Earth. The visible light imagers view sunlight that has been Thomson scattered off free electrons in the corona and interplanetary space; the theory of Thomson scattering observations has been recently reviewed by Howard & Tappin (2009a). We set out to view coronal and heliospheric events in the weeks around 2008 December, using newly developed background subtraction techniques to observe solar wind features in the HI-1 and HI-2 fields of view (DeForest et al. 2011; Howard & DeForest 2012). In the initial 36 day data set we prepared, we observed 12 disconnection events identified by a clear "V-" or "U-"shaped bright structure propagating outward in the heliosphere. We chose a particularly clearly presented one, which was easily traceable to its origin in the low corona on 2008 December 12 at 04:00, for further detailed study.

2.1. Image Preparation

Data preparation followed standard and published techniques. For COR-1 and COR-2, we downloaded Level 1

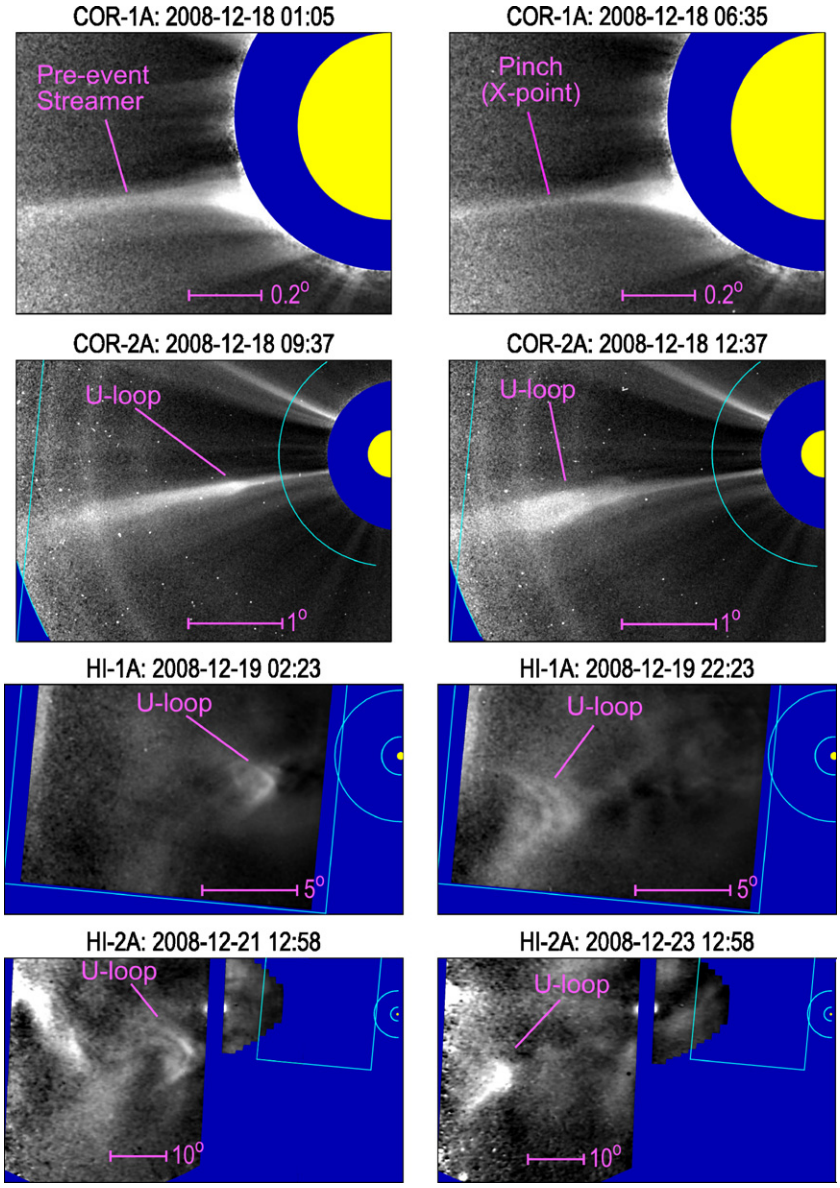

Figure 1. Disconnection event of 2008 December 18 in context—eight still images showing formation and evolution of the U-loop: left to right, top to bottom. (A color version of this figure is available in the online journal.)

(photometrically calibrated) data, and further processed them by fixed background subtraction: we acquired images for an 11 day period and found the 10 percentile value of each pixel across the entire 11 day data set. This image was median filtered over a 5×5 pixel window to generate a background image that included the F corona, any instrumental stray light, and the smooth, steady portion of the K corona. Subtracting this background from each image yielded familiar coronal images of excess feature brightness compared to the smooth, steady background. We performed one additional step: motion filtration to suppress stationary image components. This step matches the motion filtration step used for HI-1 and HI-2 (below), and suppresses the stationary streamer belt while not greatly affecting the moving features under study.

The heliospheric imagers required further processing to remove the starfield, which is quite bright compared to the faint Thomson scattering signal far from the Sun in the image plane. We processed the *STEREO A* HI-2 data as described by DeForest et al. (2011). The HI-1 data used a similar process adapted to the higher background gradients in that field of view and described by Howard & DeForest (2012).

All the imagers yielded calibrated brightness data in physical units of the mean solar surface brightness ($B_\odot = 2.3 \times 10^7\,\mathrm{W\,m^{-2}\,sr^{-1}}$). Because of the wide field of view, as a subsequent processing step we distorted the images into azimuthal coordinates, in which one coordinate is azimuth (solar position angle) in the image plane and the other is either elongation angle ϵ ("radius" on the celestial sphere) or its logarithm. The latter projection, if scaled properly, is conformal: it preserves the shape of features that are small compared to their distance from the Sun. To equalize brightness, we applied radial filters to the images for presentation, with either an $\epsilon^{3.5}$ scaling (for coronal images) or an ϵ^3 scaling (for heliospheric images).

Figure 1 shows snapshots of the disconnected plasma and associated cusp, as observed by four separate instruments over the course of four days as it propagated outward. Shortly after 2008 December 18 04:00, the streamer belt at 160° ecliptic azimuth (20° widdershins of the Sun–Earth line) pinched and

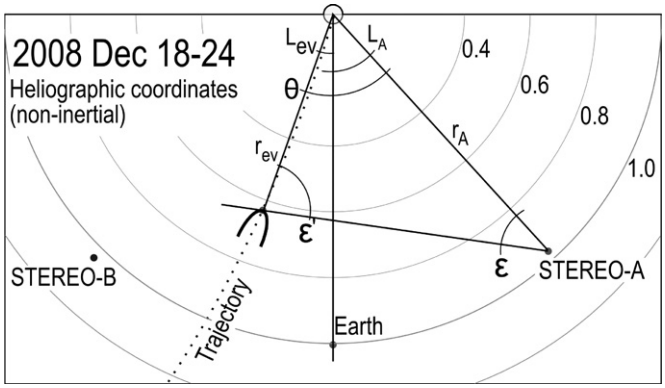

Figure 2. Observing geometry in the ecliptic plane on 2008 December 18–22.

separated, forming a "U"- loop that retracted outward, with a trailing cusp, over the course of the following three days. The feature remained visible in Thomson-scattered light because of plasma scooped up during the early acceleration period in the lower corona: this plasma remained denser than the surrounding medium, yielding a bright feature throughout the data set. The disconnected plasma completely missed the ecliptic plane and was therefore not observed in situ by any of the near-Earth or *STEREO* probes.

2.2. Observing Geometry and Three-dimensional Structure

The observing geometry for the 2008 December 18 event is shown in Figure 2, from an overhead (northward out-of-ecliptic) point of view corotating with the *STEREO A* orbit. The event departure angle was measured using direct triangulation between the coronagraphs in *STEREO A* and *STEREO B*. We used the triangulation method described by Howard & Tappin (2008). Although the disconnection event is small compared to most CMEs, subtending just a few degrees in latitude, it is still large enough to cast doubt on the simple triangulation results, so we also used "TH model" semi-empirical transient event reconstruction tool (Tappin & Howard 2009) to extract the departure angle. The TH model was developed to reconstruct CME leading edge ("sheath") overall envelope and propagation speed, but is also applicable to smaller transient events such as this one. Details, applications, and limitations of the TH model are further described by Tappin & Howard (2009) and by Howard & Tappin (2009b, 2010). Departure longitude was measured to be $-10^\circ \pm 5^\circ$ in heliographic coordinates, with an estimated event width of under 5°.

We took the disconnected feature's trajectory to have constant radial motion (the "fixed-Φ approximation") in the solar inertial frame—this leads to the slightly curved aspect to the trajectory in the corotating heliographic ecliptic frame, which maintains the prime meridian at the Earth–Sun line. Figure 2 shows an out-of-ecliptic projected view of the observing geometry, including construction angles and distances used in Section 2.4 for trajectory calculations.

2.3. Feature Evolution

To analyze the feature's evolution across a two-orders-of-magnitude shift in scale over its observed lifetime, we transformed the processed *STEREO A* source images into local heliographic radial coordinates—i.e., zero azimuth is due solar west from the viewpoint of *STEREO A*, with azimuthal coordinate increasing clockwise around the image plane; this follows early work by DeForest et al. (2001) in imaging polar plumes. Distances from Sun center are recorded as elongation angle ϵ from the center of the Sun, as a reminder of the angular nature of the wide-field observations. To avoid aliasing in the resampling process, we resampled the images using the optimized resampling package described by DeForest (2004). Figures 3 and 4 show the liftoff and propagation of the feature across 65 degrees of elongation from its origin in the solar streamer belt. Both figures have a radial gain filter applied to equalize the feature's brightness, which varies by over seven orders of magnitude: from $1.5 \times 10^{-9}\ B_\odot$ in the low streamer belt at 2008 December 18 04:30 to $5.7 \times 10^{-17}\ B_\odot$ six days later, at $\epsilon = 65^\circ$.

The bright feature takes the classic wishbone shape of reconnecting field lines emerging from a current sheet (e.g., Priest & Forbes 2000). The aspect ratio of the wishbone may be estimated by dividing the vertical height from cusp to the top of the visible horns by the width between the horns. This aspect ratio varies from ~10:1 when the horns are first clearly resolved near 2008 December 18 08:00 to approximately 2:1 some 4 hr later and 1:1 by 2008 December 19 04:00—one full day after the first pinch is observed in the streamer belt. After 2008 December 19, the feature expands approximately self-similarly as it propagates, subtending approximately 16° of azimuth and not changing its aspect ratio throughout the rest of its trajectory.

Note that aspect ratio is *not* preserved by the linear azimuthal mapping used in Figure 3, which was selected to show the early acceleration clearly; aspect ratio is preserved by the (conformal) logarithmic mapping used in Figure 4, which shows nearly self-similar expansion in the image plane despite perspective effects that come into play above about $\epsilon = 30^\circ$.

The scaling of brightness is reassuring because, in a uniformly propagating wind with no acceleration, density must decrease as r^{-2} and feature column density must thus decrease as r^{-1}, while illumination decreases as r^{-2}, so feature brightness is expected to decrease as r^{-3}. The fact that brightness levels do not change much across Figure 4, which is scaled by ϵ^3, suggests that the disconnected flux and material entrained in it are indeed propagating approximately uniformly. The fact that they *do* change slightly, with brighter images to the right, indicates that the feature is gaining intrinsic brightness by accumulating material as it propagates.

The horizontal positions and error bars in Figures 3 and 4 are the results of manual feature location of the cusp, with a point-and-click interface. The white error bars are based on the sharpness of the feature. In the excess-brightness plot, the feature is easy to see but blurs near the top of Figure 3 due to the higher levels of both photon noise and motion blur as the feature accelerates to the top of the coronagraph field of view. The running-difference plot highlights fine scale feature and helps identify the cusp location near the top of the COR-2 field of view.

2.4. Acceleration Profile

Converting angular observed coordinates to examine the inertial behavior of the plasma requires triangulation using the law of sines. Using the "fixed-Φ" approximation (assuming the feature's cusp is small and that it propagates in a radial line from the Sun), the feature's radius from the Sun is easily calculated:

$$r_{\rm ev} = r_A \frac{\sin(\epsilon')}{\sin(\epsilon)}, \quad (1)$$

where the variables take the meanings in Figure 2: ϵ is the solar elongation of the feature as seen from *STEREO A*, ϵ' is

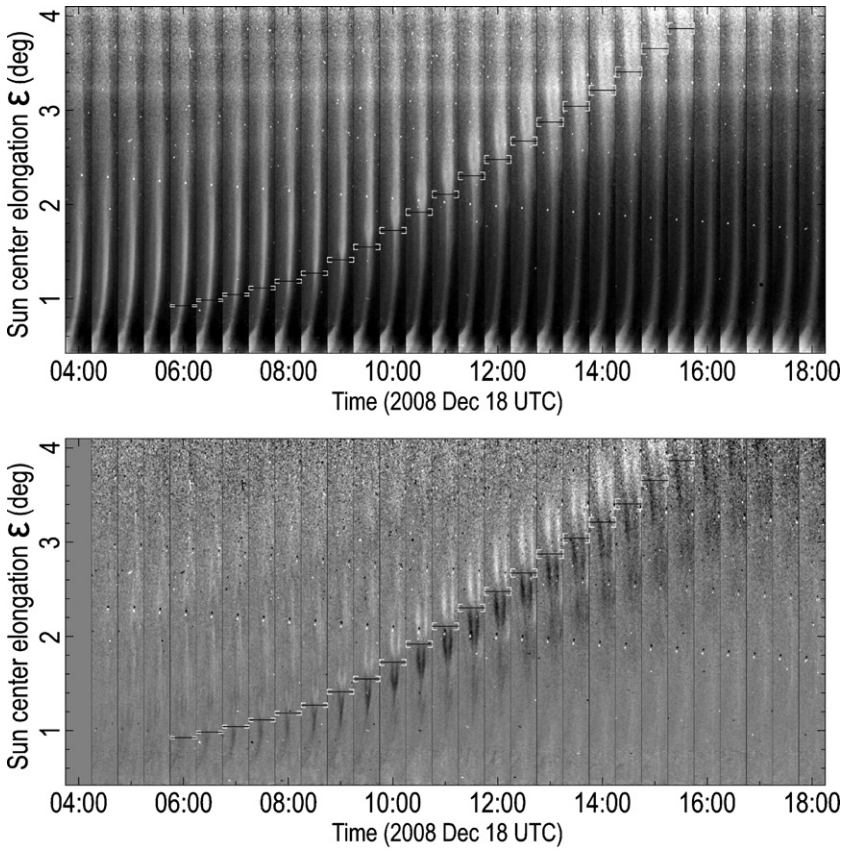

Figure 3. Formation and early acceleration of the 2008 December 18 disconnection event through the *STEREO A* COR-1 and COR-2 fields of view. The trailing edge of the event is marked, with error bars based on feature identification. Top: direct excess-brightness images show feature formation and overall structure. Bottom: running-difference images show detail. These stack plots include a small image of the feature at each sampled time to show evolution. Intensities are scaled by $\epsilon^{3.5}$ to equalize brightness vs. height. The individual images have been resampled into linear azimuthal (radial) coordinates, and the horizontal range is 160°–174° of azimuth. Note that this projection does not preserve aspect ratio: despite appearances, the event widens as it rises.

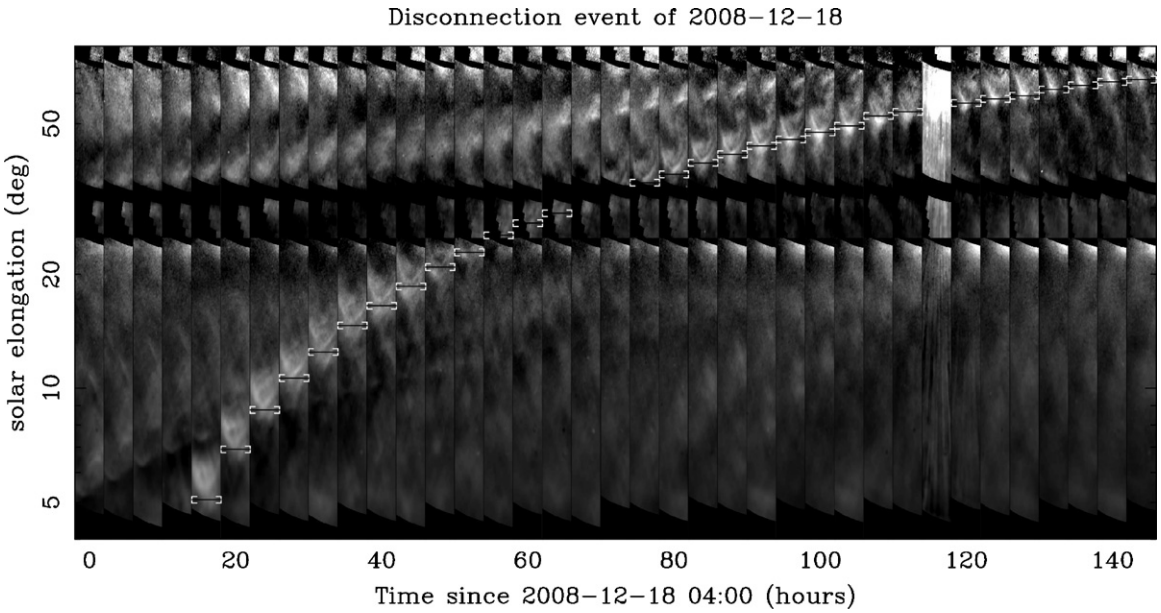

Figure 4. Propagation and evolution of the 2008 December 18 disconnection event through the *STEREO A* HI-1 and HI-2 fields of view. The trailing edge of the event is marked, with error bars based on feature identification. These stack plots include a small image of the feature at each sampled time to show evolution. The individual images have been resampled into logarithmic azimuthal (radial) coordinates, and the horizontal range is 162°–178° of azimuth. This projection is conformal, so the shape of the feature is preserved in each image. Intensities are scaled by ϵ^3 to equalize brightness vs. height. Note self-similar expansion: the angular width and shape of the feature are preserved.

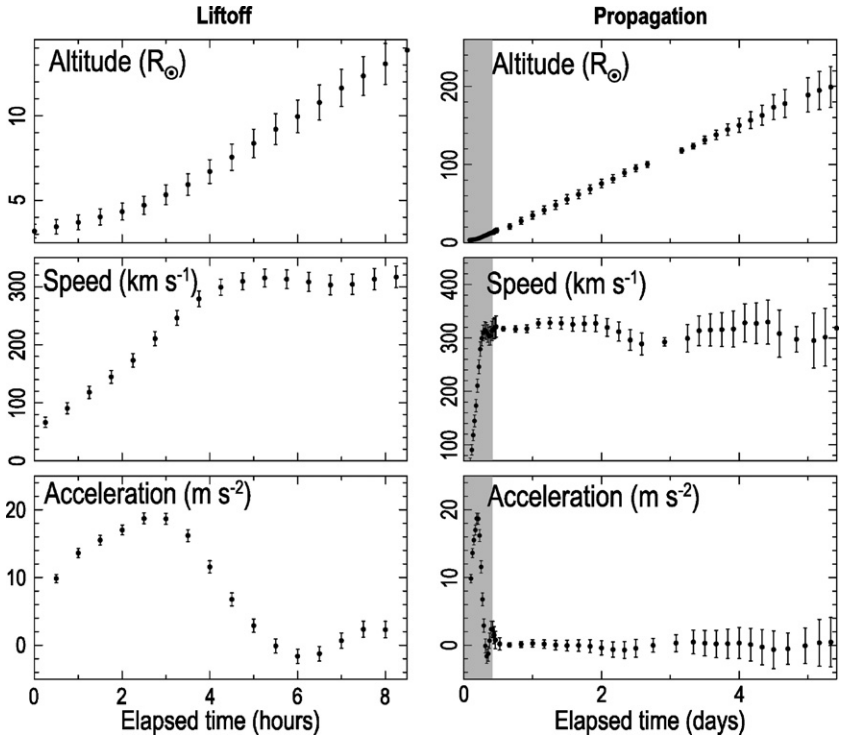

Figure 5. Inferred position, speed, and acceleration of the disconnected plasma from the 2008 December 18 event, during onset (left) and over the full observation period (right). Error bars are derived by propagating a priori location error and geometric error in the longitude of the event. The shaded region indicates the full time range of the left-side plots.

the solar elongation of *STEREO A* as seen from the feature, and the *STEREO A* solar distance r_A is found by spacecraft tracking and is supplied by the mission. Although no camera was present at the event itself, ϵ' is calculated by noting that $\epsilon' = 180^\circ - \epsilon - (L - L_{\rm ev})$ as the feature, *STEREO A,* and the Sun form a triangle. Figure 5 shows the results of the tracking from Figures 3 and 4, propagated through Equation (1).

As expected, the event rapidly accelerates during the early phase, reaching a peak acceleration of $20\,{\rm m\,s^{-2}}$ as the aspect ratio changes in the initial hours. The acceleration peaks 4–5 hr after the initial pinch in the streamer belt or 2–3 hr after the first observation of a well-formed cusp. The feature reaches its final speed of $\sim 320 \pm 15\,{\rm km\,s^{-1}}$ within just 8 hr of the initial pinch at 04:00 and within 6 hr of the first observation of the well-formed cusp at 06:00, and undergoes no further significant acceleration nor deceleration during its observed passage to beyond 1 AU over the next five days.

2.5. Mass Profile

We extracted photometric densities using the feature brightness in suitable frames. The feature brightness is determined from the density via the Thomson scattering equation (see, e.g., Howard & Tappin 2009a for a clear exposition). Compact features can be treated as nearly point sources, and the line-of-sight integral for the optically thin medium reduces to

$$B = B_\odot \Omega_\odot(r) \sigma_e (1 + \cos^2 \chi) \rho \mu_{\rm av}^{-1} d, \qquad (2)$$

where B is the measured feature brightness (in units of emissivity: $\rm W\,m^{-2}\,sr^{-1}$); $B_\odot$ is (still) the solar surface brightness; $\Omega_\odot(r)$ is the solid angle subtended by the Sun at the point of scatter, well approximated by $\pi r_\odot^2 r_{\rm ev}^{-2}$ everywhere above about $4\,r_\odot$; σ_e is the differential Thomson scattering cross section, given by half of the square of the classical electron radius $r_e^2/2 = 4.0 \times 10^{-30}\,{\rm m}^2$; χ is the scattering angle (equal to ϵ' in Figure 2); ρ is the mass density; $\mu_{\rm av}$ is the average mass per electron in the coronal plasma; and d is the depth of the feature.

$mu_{\rm av}$ may be calculated from the spectroscopically measured 5% He/H number ratio in the corona (Laming & Feldman 2001) and the assumption that the helium is fully ionized (yielding two electrons per ion). This yields $mu_{\rm av} = 1.1 m_p = 1.84 \times 10^{-27}\,{\rm kg}$.

Solving for the line-of-sight integrated mass surface density ρd gives

$$\rho d = \mu_{\rm av} \frac{B}{B_\odot} \Omega_\odot^{-1}(r) \sigma_e^{-1} (1 + \cos^2 \epsilon')^{-1} \qquad (3)$$

and therefore

$$m_{\rm ev} = (\rho d)\, wh = \mu_{\rm av} \frac{B}{B_\odot} \Omega_\odot^{-1}(r) \sigma_e^{-1} (1 + \cos^2 \epsilon')^{-1} \times \Omega_{\rm ev} S^2, \qquad (4)$$

where w and h are the dimensions shown in Figure 7; $\Omega_{\rm ev}$ is the solid angle subtended by the feature in the images; and S is the calculated spacecraft–feature distance, calculated by the law of sines as for $r_{\rm ev}$.

To extract the mass profile from the data, we generated an image sequence containing the feature and marked the locus of the feature visually using a pixel paint program. Using the generated masks, we summed masked pixels in the feature for each photometric image, thereby integrating the feature brightness over the solid angle represented by the corresponding pixels, to obtain an intensity and an average brightness within the feature. To account for errors in visual masking, we assigned error bars based on one-pixel dilation and one-pixel contraction of the masked locus. We omitted frames with excessive noise,

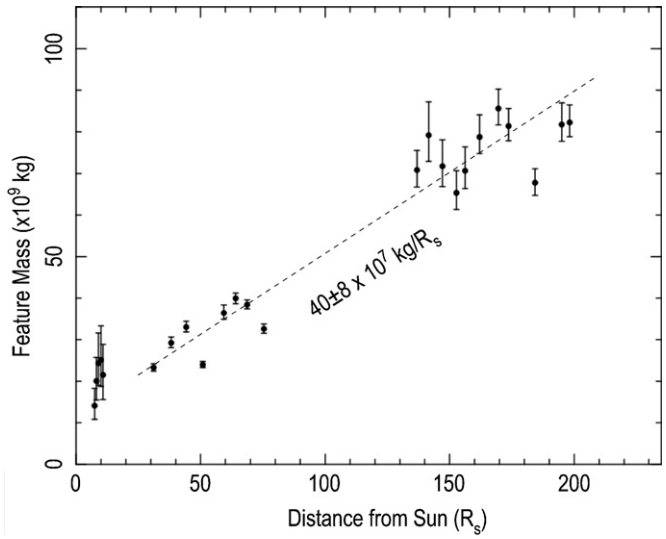

Figure 6. Photometrically determined excess mass profile of the retracting disconnected feature of 2008 December 18. Error bars are based on identification of the feature boundary in the images. The trendline is extracted from regression of the HI-1 and HI-2 data. The mass shown is excess mass in the feature compared to the background solar wind (see the text).

encroachment of an image boundary, or a star or cosmic ray in or near the feature. The results of the calculation are given in Figure 6, which shows steady accretion of material through most of the journey through the heliosphere.

Because our photometric analysis is based on subtraction of a calculated background derived from the data set itself, we measure only excess feature brightness (not absolute brightness) from Thomson scattering; thus our brightness measurements and mass estimates are biased low, because we cannot measure the absolute density of the background. The initial derived mass of 20–25 Tg translates to an electron number density of 2×10^7 cm^{-3} in the lower corona, which is comparable to the density in bright coronal features—so the total mass may be up to a factor of order two higher.

The final "feature excess" mass is $8 \pm 2 \times 10^{10}$ kg, and the final subtended solid angle is 0.028 sr, for a presented cross section of $4.3 \pm 0.1 \times 10^{20}$ m^2. Taking the depth to be the square root of the observed cross section yields an estimated volume at 1 AU of $8.9 \pm 0.3 \times 10^{31}$ m^3, for a total estimated excess electron density of 5 ± 1.4 cm^{-3} at 1 AU, which is in good agreement with slow solar wind densities (3–10 cm^{-3} when scaled to 1 AU) that were observed by *Ulysses* in situ in the same heliographic latitude range (e.g., McComas et al. 2000). Approximately 2/3 of this excess density appears to have been accumulated en route from the surrounding solar wind; this is further described in Section 2.7.

2.6. Entrained Magnetic Flux

From the mass of the feature, and its acceleration, it is possible to extract the entrained magnetic field by measuring the rate of change of momentum and inferring a magnetic tension force via $f = ma$. The system is sketched in Figure 7. The magnetic tension force is conserved along the open field lines, so we can calculate it at any convenient cut plane including the one shown. Tension force is frequently referred to as a "curvature force" and calculated locally; here we integrate around the "U" and note that the integrated force is just the unbalanced tension on the field lines contained in the "U" shape. It is therefore

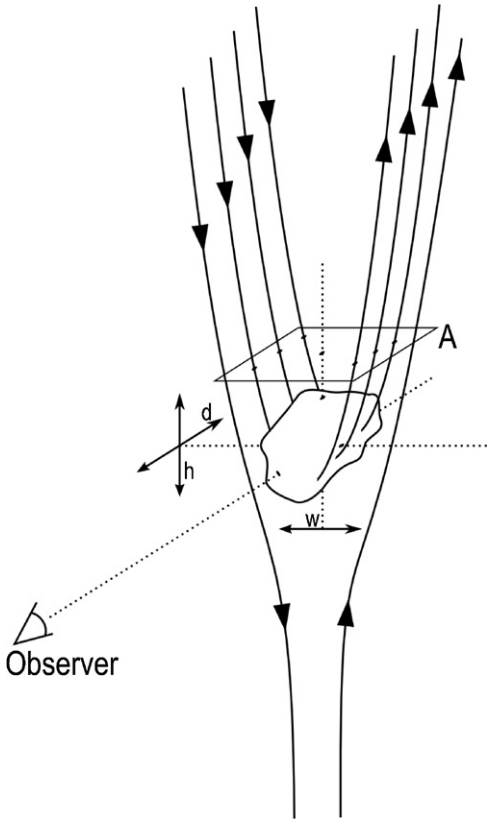

Figure 7. Cartoon of the initial acceleration process of a disconnection event. Tension force along newly released field lines is balanced by mass entrained on the field lines. By measuring the acceleration and mass we infer the amount of magnetic flux that was disconnected.

given by

$$f = m_{\rm ev} a_{\rm ev} = f_B = \frac{B^2 A}{2\mu_0} = \frac{\Phi^2}{2\mu_0 A}, \tag{5}$$

where B is the magnetic field strength (not brightness, as before). Solving for Φ,

$$\Phi = \sqrt{2\mu_0 d w m_{\rm ev} a_{\rm ev}}, \tag{6}$$

taking $m_{\rm ev}$ to be 25 Tg (2.5×10^{10} kg) during the peak of the acceleration and taking $w = d = 0.2\,R_\odot$ (based on the measured width of the feature's fork during maximum acceleration, at $6R_s$ from the surface ($7R_s$ from Sun center)) gives $\Phi = 1.6 \times 10^{11}$ Wb (1.6×10^{19} Mx), corresponding to an average field strength of 8 μT (0.08 G) at that altitude, or an equivalent r^2-scaled field of 400 μT (4 G) at the surface; this is comparable to accepted values of the open flux density at the solar surface at solar minimum. Because of the way m was calculated (Section 2.5 above) this figure is probably low by a factor of order $\sqrt{2}$.

2.7. Accretion and Force Balance

As the disconnected structure travels outward, it accretes new material. This effect is dramatic: as seen in Figure 6, the mass increases by a factor of three from the corona to 1 AU. We conjecture that the material is accreted by "snowplow" effects from the plasma ahead of the disconnected cusp as it propagates. For the observed mass growth in the feature, new material must be compressed to become visible in our Thomson scattering images, and the most plausible way for it to be compressed is via

ram effects. This scenario also neatly explains the constant speed of the feature, by balancing the continued tension force from the cusp with accretion momentum transfer. Here we explore the concept of force balance between accretion and the tension force to identify whether some other model is required in addition to this simple one.

Extending Newton's law to include momentum transfer by accretion, and neglecting all but the tension force,

$$\frac{\Phi^2}{2\mu_0 A_\Phi} = m_{\rm ev} a_{\rm ev} + \frac{dm_{\rm ev}}{dt}\Delta v, \tag{7}$$

where the left-hand side is just the tension force from Equation (5), with the modification that the cross section of the exiting field lines is written A_Φ; $a_{\rm ev} = 0$ after the initial acceleration; and the second term represents momentum transfer into accreted material, with Δv being the difference between the feature speed and surrounding wind speed. The feature is thus in equilibrium between accretion drag and continued acceleration by the tension force. This accretion drag is important to the observed increase in feature mass, because ram pressure against the surrounding wind material is what compresses incoming material and renders it visible in the data against the subtracted background.

Applying conservation of mass, we can relate Δv and the average density of the background solar wind through which the feature is propagating:

$$\rho_{\rm sw} = \frac{dm_{\rm ev}/dt}{A_{\rm ev}\Delta v}, \tag{8}$$

where $A_{\rm ev}$ is the geometrical area presented by the feature to the slow wind ahead of it. Solving Equations (7) and (8) to eliminate Δv gives

$$\rho_{\rm sw} = \left(\frac{dm_{\rm ev}}{dt}\right)^2 \left(\frac{2\mu_0}{\Phi^2}\right)\left(\frac{A_\Phi}{A_{\rm ev}}\right), \tag{9}$$

which gives the background solar wind density in terms of the accumulation rate of mass in the observed feature, assuming constant outflow for both the wind and the feature, and acceleration by the tension force. Given the conservation of mass and the approximately constant speed of the solar wind, $\rho_{\rm sw}$ falls as approximately r^{-2}. Further, we observe nearly self-similar expansion throughout most of the heliospheric range, so $A_\Phi/A_{\rm ev}$ is constant in that part of the trajectory—hence $dm_{\rm ev}/dt$ must also fall as r^{-1} during the approximately constant speed portion of the feature's lifetime. Using this functional form, we can extract an analytic expression for the feature mass versus radius. We introduce the r^{-1} dependence by switching from the linear regression used in Figure 6 to a semi-log regression that assumes $dm_{\rm ev}/d(\log_e(r))$ to be constant. Figure 8 shows such a regression, with the result that $dm_{\rm ev}/dr = 34 \pm 3 \times 10^9\,(R_\odot/r)$ kg $R_\odot^{-1}$. Including the measured outflow speed of $315 \pm 15\,{\rm km\,s^{-1}}$, we find that $dm_{\rm ev}/dt = (1\,{\rm AU}/r)(7.1 \pm 1 \times 10^4\,{\rm kg\,s^{-1}})$.

Including all of these values in Equation (9), together with the average particle mass from Section 2.5, yields a background wind numeric density of $n_{\rm sw}$ (1 AU) of $30 \pm 6\,{\rm cm^{-3}}\,(A_\Phi/A_{\rm ev})$. From the morphology of the feature in Figure 4, we conservatively estimate $A_\Phi/A_{\rm ev} < 0.25$, i.e., the forward cross section of the "horns" of the V appears to be well under 1/4 of the cross section of the V itself. This value yields a derived background solar wind density of $n_{\rm sw} < 8\,{\rm cm^{-3}}$ at 1 AU to maintain the force balance in Equation (7). That figure is again in line with the wind measurements from *Ulysses* at 15° heliographic latitude (McComas et al. 2000), adding to the plausibility of the accretion force balance picture. The corresponding mass density limit is $\rho_{\rm sw} < 8 \times 10^{-19}\,{\rm kg\,m^{-3}}$ at 1 AU.

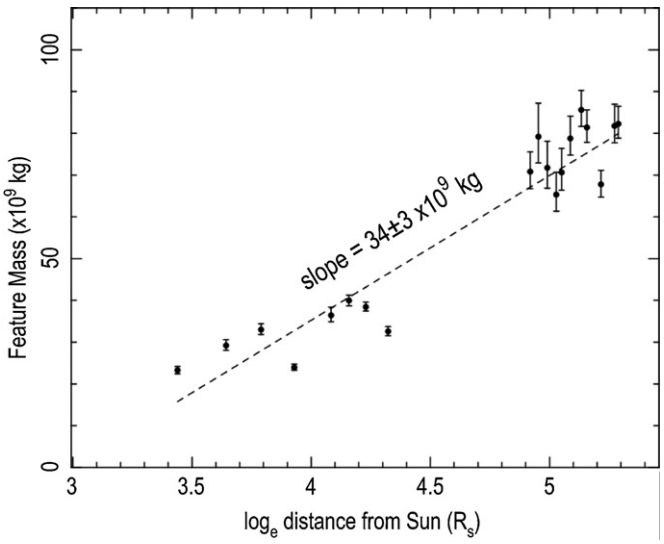

Figure 8. Semi-log regression fit of $m_{\rm ev}(r)$.

As a sanity check, we can use this $\rho_{\rm sw}$ limit and Equation (8) to find that Δv must then be a few tens of ${\rm km\,s^{-1}}$, i.e., the background wind speed must be close to $300\,{\rm km\,s^{-1}}$.

We conclude that the picture of force balance between snowplow accretion and the tension force is at least broadly consistent with the observed feature, though further study of more events (preferably with corresponding in situ measurements of the feature itself) is necessary.

3. DISCUSSION

Using data from *STEREO*/SECCHI, we have identified and measured the characteristics of a single flux disconnection event and associated cusp feature, similar to that discovered by McComas et al. (1992), from initial detection in the lower corona to distances beyond 1 AU. The cusp feature is formed in the classic X-point geometry and rapidly accelerates under the tension force to approximately $320\,{\rm km\,s^{-1}}$, which it reaches in under 4 hr at an altitude of approximately 10 $R_\odot$. Thereafter, the feature continues to accumulate mass but maintains approximately constant speed until it is lost to sight 1.2 AU from the Sun.

Based on photometry, we are able to estimate the onset mass of the event as 25 Tg and the entrained flux as 160 G Wb, corresponding to a coronal field strength of 0.08 G and an r^2-normalized surface open field of 4 G over the projected surface footprint of the feature. These estimates are likely low by a factor of order $\sqrt{2}$, because they make use of feature excess brightness rather than absolute Thomson-scattered brightness in the coronagraph images; using polarized-brightness imagery could improve the measurement by separating the non-transient component of the Thomson scattering signal from the unwanted F coronal background.

Because our measurements are all based on morphology and photometry, we have performed several consistency checks to build confidence in the calculated parameters of the feature as it propagates. In particular, a model of simple force balance between the tension force and mass accretion is consistent

with both the inferred magnetic field and accepted values for background slow solar wind density and speed.

Simple accretion models such as we developed here demonstrate clearly why ejected features such as U-loops or CMEs seem frequently to propagate at near constant speed: under continuous weak driving, an equilibrium forms rapidly between the driving force and momentum transfer by mass accretion. The equilibrium outflow speed is the sum of a large, fixed (or at least driver-independent) speed—that of the surrounding wind—with a smaller offset speed that drives mass accretion. Thus the feature speed is quite insensitive to the driver. In our case, doubling the tension force would only increase the outflow rate by ∼5%.

The event under study is well presented, but is not unusual at all; such events are easy to identify in heliospheric image sequences, because of their distinctive "U" and cusp shape; they are readily traced back to the corona. This technique represents a new, very effective way of finding these disconnection events, which are small and hard to identify in the coronagraph sequences alone, but are strongly and easily visible in the processed heliospheric images.

In an initial reduced data set of 36 days near the deepest part of the recent extended solar minimum (2008 December–2009 January), we identified 12 such events; all of them were identified by tracking "V" or "U" shapes back from the heliospheric images to the corona. Assuming the present feature to be typical, and considering that the single viewpoint affords clear coverage of about 1/4 of the circumference of the Sun, we estimate the global disconnection feature rate at that time to be over 1 event day^{-1}, and the flux disconnection rate to thus be at least of order 60 T Wb yr^{-1}. Expanded to a 1 AU sphere, this amounts to a rate of change of the open field of order 0.2 nT yr^{-1}, which is a significant fraction of the observed cycle-dependent rate of change of the open heliospheric field (e.g., Schwadron et al. 2010). These figures are based on a single calculated flux and an event rate obtained by initial visual inspection of a single 36 day data set, and hence are merely rough estimates—but they indicate that flux disconnections of this type are important to the global balance of open flux. Further study, in the form of a systematic survey, is needed to determine whether they are the primary mechanism of flux disconnection from the Sun.

The authors thank the *STEREO* instrument teams for making their data available. Our image processing made heavy use of the freeware Perl Data Language (http://pdl.perl.org). The work was enhanced by enlightening conversations with J. Burkepile, C. Eyles, and N. Schwadron, to whom we are indebted. This work was supported by NASA's SHP-GI program, under grant NNG05GK14G.

REFERENCES

Cliver, E. W. 1989, Sol. Phys., 122, 319
DeForest, C. E. 2004, Sol. Phys., 219, 3
DeForest, C. E., Howard, T. A., & Tappin, S. J. 2011, ApJ, 738, 103
DeForest, C. E., Plunkett, S. P., & Andrews, M. D. 2001, ApJ, 546, 569
Gosling, J. T. 1990, in Physics of Magnetic Flux Ropes, ed. L. C. Lee (Geophysical Monograph Ser. 58; Washington, DC: American Geophysical Union), 343
Gosling, J. T. 1993, J. Geophys. Res., 981, 18937
Gosling, J. T., Hildner, E., MacQueen, R. M., et al. 1974, J. Geophys. Res., 79, 4581
Howard, R. A., Moses, J. D., Vourlidas, A., et al. 2008, Space Sci. Rev., 136, 67
Howard, T. A., & DeForest, C. E. 2012, ApJ, in press
Howard, T. A., & Tappin, S. J. 2008, Sol. Phys., 252, 373
Howard, T. A., & Tappin, S. J. 2009a, Space Sci. Rev., 147, 31
Howard, T. A., & Tappin, S. J. 2009b, Space Sci. Rev., 147, 89
Howard, T. A., & Tappin, S. J. 2010, Space Weather, 80, S07004
Hundhausen, A. J. 1993, J. Geophys. Res., 981, 13177
Laming, J. M., & Feldman, U. 2001, ApJ, 546, 552
Linker, J. A., van Hoven, G., & McComas, D. J. 1992, J. Geophys. Res., 971, 13733
McComas, D. J. 1994, NASA STI/Recon Technical Report N, 951, 10770
McComas, D. J. 1995, Tongues, Bottles, and Disconnected Loops: The Opening and Closing of the Interplanetary Magnetic Field (95RG00124), Tech. Rep.
McComas, D. J., Barraclough, B. L., Funsten, H. O., et al. 2000, J. Geophys. Res., 105, 10419
McComas, D. J., Ebert, R. W., Elliott, H. A., et al. 2008, Geophys. Res. Lett., 351, L18103
McComas, D. J., Gosling, J. T., & Phillips, J. L. 1992a, J. Geophys. Res., 97, 171
McComas, D. J., Gosling, J. T., & Phillips, J. L. 1992b, in Solar Wind Seven Colloquium, ed. E. Marsch & R. Schwenn (Oxford: Pergamon), 643
McComas, D. J., Gosling, J. T., Phillips, J. L., et al. 1989, J. Geophys. Res., 94, 6907
McComas, D. J., Phillips, J. L., Hundhausen, A. J., & Burkepile, J. T. 1991, Geophys. Res. Lett., 18, 73
McComas, D. J., Phillips, J. L., Hundhausen, A. J., & Burkepile, J. T. 1992c, in Solar Wind Seven Colloquium, ed. E. Marsch & R. Schwenn (Oxford: Pergamon), 225
Priest, E. R., & Forbes, T. G. 2000, in Encyclopedia of Astronomy & Astrophysics, ed. P. Murdin (Boca Raton, FL: Taylor and Francis)
Schwadron, N. A., Connick, D. E., & Smith, C. 2010, ApJ, 722, L132
Slavin, J. A., Jungman, G., & Smith, E. J. 1986, Geophys. Res. Lett., 13, 513
Smith, E. J., & Balogh, A. 2008, Geophys. Res. Lett., 352, L22103
St. Cyr, O. C., & Burkepile, J. T. 1990, NASA STI/Recon Technical Report N, 911, 17996
Tappin, S. J., & Howard, T. A. 2009, Space Sci. Rev., 147, 55
Tousey, R. 1973, in Space Research XIII, Vol. 2, ed. M. J. Rycroft & S. K. Runcorn (Weinheim: Wiley-VCH), 713